# Quantum-Dot Lasers—Desynchronized Nonlinear Dynamics of Electrons and Holes

Kathy Lüdge and Eckehard Schöll

Abstract—We analyze the complex turn-on behavior of semiconductor quantum-dot (QD) lasers in terms of a nonlinear rate equation model for the electron and hole densities in the QDs and the wetting layer, and the photons. A basic ingredient of the model is the nonlinearity of the microscopic carrier—carrier scattering rates. With the framework of detailed balance, we analytically relate the microscopic in- and out-scattering rates. We gain insight into the anomalous nonlinear dynamics of QD lasers by a detailed analysis of various sections of the 5-D phase space, accounting for density-dependent carrier scattering times. We show that the strongly damped relaxation oscillations are characterized by a desynchronization of electron and hole dynamics in the dots. Analytic approximations for the steady-state characteristics are also derived.

Index Terms—Nonlinear relaxation oscillations (ROs), quantum-dot (QD) lasers, turn-on dynamics.

#### I. INTRODUCTION

UANTUM-DOT (QD) injection lasers, which are singled out by low threshold current, low bit error rate, and large temperature stability, are an important optoelectronic application of self-organized semiconductor QD structures [1], [2]. In previous works [3]–[5], it was shown that the nonlinear dynamic response of QD lasers can be quantitatively understood by including the strongly nonlinear character of electron-electron scattering processes between the QDs and the 2-D wetting layer (WL) [6] into a rate equation model. Due to an error in the sign of the QD energies in the numerical code, the scattering rates in [3]-[5] were erroneously based on an energy scheme where the QD levels are in resonance with the WL, which is not the normal configuration. In this paper, we present correct scattering rates, and furthermore, discuss in detail the resulting gain switching dynamics of the laser. While the internal kinetics of QD and WL electrons and holes depend sensitively upon the scattering rates, the turn-on dynamics of the optical output is essentially the same as in [3]–[5].

Compared to other rate equation models that include scattering rates that are linear in the WL density and equal for electrons and holes [7]–[12], we emphasize the importance of different nonlinear rates for both types of carriers for the internal laser dynamics. Following a dynamic hierarchy, our model bridges the gap between a fully microscopic description,

Manuscript received April 08, 2009; revised July 01, 2009. Current version published October 28, 2009. This work was supported by the Deutsche Forschungsgemeinschaft within Sfb 787.

The authors are with the Institut für Theoretische Physik, Technische Universität Berlin, 10623 Berlin, Germany (e-mail: luedge@physik.tu-berlin.de).

Color versions of one or more of the figures in this paper are available online at http://ieeexplore.ieee.org.

Digital Object Identifier 10.1109/JQE.2009.2028159

including polarization and population dynamics [13]–[15], and rate equations with constant coefficients. In [11] and [16], different scattering times are included for electrons and holes, and the resulting asymmetry is discussed, but their scattering times are constant parameters. Following the argument of mass action kinetics in nondegenerate semiconductors, Auger processes depend quadratically on the WL densities [17], [18], as assumed in [19] to discuss the effect of optical feedback and in [20] to interpret experimental results. However, we show that depending on the carrier densities in the WL, the scattering rates show a more complex dependence that is different for electrons and holes. We also derive a detailed balance formula connecting the nonequilibrium in- and out-scattering rates via a WL-carrier-density-dependent factor. The effect of inhomogeneous broadening, as discussed in [7], [21], and [22], which was shown to be important in order to discuss the linewidth-enhancement factor [9] or mode-locking effects [23], is taken into account in a simplified approach that distinguishes only between the total QD density and the density of the lasing subgroup of QDs whose size matches with the laser mode.

We can relate the experimentally found low cutoff frequency and the strong damping of relaxation oscillations (ROs) of these lasers to the microscopic scattering processes. It is the purpose of this paper to provide insight into the dynamics by developing analytic approximations based upon a microscopic model. The quasi-steady state reached during turn-on permits us to simplify parts of the nonlinear scattering rates and allows for insights into the physical processes.

This paper is organized as follows. In Section II, we present the rate equation model and discuss basic properties of the nonlinear scattering rates used for the simulations. Subsequently, in Section III, we analyze the laser turn-on dynamics and the differences in the dynamics of electrons and holes. In Section IV, analytic results for the steady-state behavior of the laser will be presented, before we conclude in Section V.

## II. QD LASER MODEL

The analytic and numeric investigations of the laser turn-on dynamics presented here are based on the model given in [5]. However, there are differences in the model discussed here that concern the parameter values, the incorporation of inhomogeneous broadening, and a different energy scheme of the device. In the QD laser system, the electrons are first injected into a WL before they are captured by the QDs. We consider a two-level system for electrons and holes in the QDs with an energy separation of  $\hbar\omega=0.96$  eV as common for self-organized QDs in the InAs/InGaAs material system. The following nonlinear rate equations [see (1)–(5)] for the charge carrier densities in the QDs,  $n_e$  and  $n_h$ , the carrier densities in the WL,  $w_e$  and  $w_h$ 

(e and h stand for electrons and holes, respectively), and the photon density  $n_{vh}$  determine the dynamics:

$$\dot{n}_e = -\frac{1}{\tau_e} n_e + S_e^{\text{in}} N^{\text{QD}} - R_{\text{ind}}(n_e, n_h, n_{ph}) - R_{\text{sp}}(n_e, n_h)$$
(1)

$$\dot{n}_h = -\frac{1}{\tau_h} n_h + S_h^{\text{in}} N^{\text{QD}} - R_{\text{ind}}(n_e, n_h, n_{ph}) - R_{\text{sp}}(n_e, n_h)$$

$$\dot{w}_e = \eta \frac{j(t)}{e_o} + \frac{n_e}{\tau_e} \frac{N^{\text{sum}}}{N^{\text{QD}}} - S_e^{\text{in}} N^{\text{sum}} - \tilde{R}_{\text{sp}}(w_e, w_h)$$
(3)

$$\dot{w}_h = \eta \frac{j(t)}{e_o} + \frac{n_h}{\tau_h} \frac{N^{\text{sum}}}{N^{\text{QD}}} - S_h^{\text{in}} N^{\text{sum}} - \tilde{R}_{\text{sp}}(w_e, w_h)$$
(4)

$$\dot{n}_{ph} = -2\kappa n_{ph} + \Gamma R_{\rm ind}(n_e, n_h, n_{ph}) + \beta R_{\rm sp}(n_e, n_h). \tag{5}$$

The induced processes of absorption and emission are modeled by a linear gain  $R_{\rm ind}(n_e,n_h,n_{ph})=WA(n_e+n_h-N^{\rm QD})n_{ph}$ , where  $N^{\rm QD}$  denotes twice the QD density of the lasing subgroup (the factor of 2 accounts for spin degeneracy),  $W = (|\mu|^2 \sqrt{\varepsilon_{bg}})/(3\pi\varepsilon_0\hbar)(\omega/c)^3$  is the Einstein coefficient, and A is the WL normalization area. The density  $N^{\text{sum}}$  is twice the total QD density as given by experimental surface imaging. The spontaneous emission in the QDs is approximated by  $R_{\rm sp}(n_e,n_h)=(W/N^{\rm QD})n_en_h$ . The WL spontaneous recombination rate is expressed by  $\tilde{R}_{\rm sp}(w_e,w_h)=B^Sw_ew_h$ , where  $B^S$  is the band–band recombination coefficient in the WL.  $\beta$  is the spontaneous emission coefficient and  $\Gamma = \Gamma_q N^{\rm QD}/N^{\rm sum}$  is the optical confinement factor.  $\Gamma$  is the product of the geometric confinement factor  $\Gamma_g$  (i.e., the ratio of the volume of all QDs and the mode volume) and the ratio  $N^{\rm QD}/N^{\rm sum}$  (accounting for reduced gain because, due to the size distribution of the QDs, only a subgroup of all QDs match the mode energy for lasing). The coefficient  $2\kappa$  expresses the total cavity loss. The variable j is the injection current density,  $e_o$  is the elementary charge, and  $\eta = 1 - w_e/N^{\rm WL}$  is the injection efficiency that accounts for the fact that we cannot inject any more carriers if the WL is already filled ( $w_e = N^{\text{WL}}$ ). The spectral properties of the laser output are not addressed in the model, as the photon density is an average over all longitudinal modes. Changes in the QD size distribution are taken into account only by changes in the active QD density, which basically changes the gain. The values of parameters used in our simulations are listed in

A crucial contribution to the dynamics of QD lasers is given by the nonradiative carrier–carrier scattering rates  $S_e^{\rm in}$  and  $S_h^{\rm in}$  for electron and hole capture into the QD levels,  $S_e^{\rm out}$  and  $S_h^{\rm out}$  for carrier escape from the QD levels, and scattering times  $\tau_e = (S_e^{\rm in} + S_e^{\rm out})^{-1}$  and  $\tau_h = (S_h^{\rm in} + S_h^{\rm out})^{-1}$ . The rates are determined microscopically within the Boltzmann equation and orthogonalized plane-wave approach [4]. All electron–electron, hole–hole, and mixed electron–hole Auger processes are included in the rates [5]. The Coulomb interaction is considered up to the second order in the screened Coulomb potential. The calculated scattering rates depend in a strongly nonlinear way upon the WL carrier densities  $w_e$  and  $w_h$  [4], [5]. The curves in Fig. 1(a) and (b) show the in- and out-scattering rates for electrons and holes, respectively. Note that the values for electron and hole in-scattering rates differ by about a factor of 2

TABLE I
NUMERICAL PARAMETERS USED IN THE SIMULATION
UNLESS STATED OTHERWISE

symbol	value	symbol	value
$\overline{W}$	$0.7  ns^{-1}$	A	$4 \times 10^{-5}  cm^2$
T	300 K	$N^{QD}$	$0.6 \times 10^{10} cm^{-2}$
$2\kappa$	$0.1  ps^{-1}$	$N^{sum}$	$20\times10^{10}cm^{-2}$
$\Gamma_g$	0.075	$N^{WL}$	$2\times10^{13}cm^{-2}$
Γ	$2.25\times10^{-3}$	$B^S$	$850  ns^{-1}  nm^2$
$\mu$	$0.75e_0nm$	β	$5\times 10^{-6}$
$arepsilon_{bg}$	14.2	$m_{e}\left(m_{h}\right)$	$0.043(0.45)m_0$
$\Delta E_e$	190 <i>meV</i>	$\Delta E_h$	69 meV

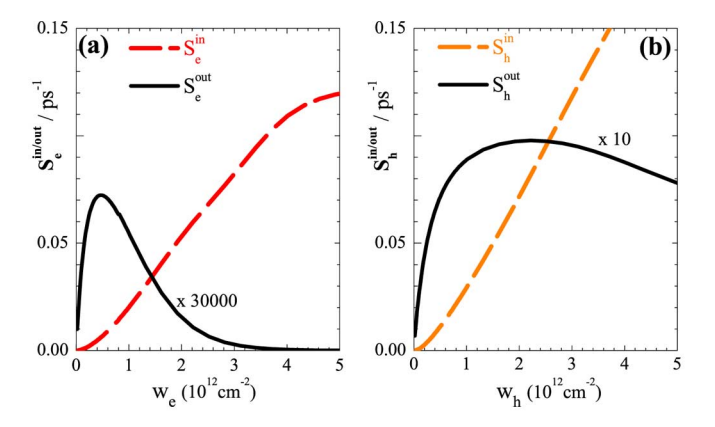


Fig. 1. Carrier–carrier scattering rates. (a) Dashed red and solid black lines show electron in- and out-scattering rates  $S_e^{\rm in}$  and  $S_e^{\rm out}$ , respectively, as a function of the WL electron density  $w_e$ . (b) Dashed orange and solid black lines depict in- and out-scattering rates for holes as a function of the WL hole density  $w_h$ . The ratio  $g_c = w_h/w_e$  is fixed to 1.5.

and the out-scattering rates differ by two orders of magnitude. For very low WL carrier densities, the in-scattering rate shows a quadratic increase as predicted by mass action kinetics, but it deviates from this functional relation for increasing WL carrier densities. The out-scattering is characterized by a sharp increase with increasing density of scattering partners followed by a decrease that is caused by Pauli blocking of the WL states. Since the holes have a larger effective mass, the maximum of the out-scattering rate lies at higher WL carrier densities than for electrons and is outside the range shown in Fig. 1(b). Due to the mixed electron-hole scattering processes, the rates depend on both  $w_e$  and  $w_h$ , which would require a plot of  $S_{e/h}^{\rm in/out}(w_e,w_h)$ for complete information. In Fig. 1, we fixed the ratio  $g_c =$  $w_h/w_e$  to  $q_c = 1.5$  in order to visualize the rates. However, for the numeric simulations of the laser dynamics, the full dependence of the scattering rates on both  $w_e$  and  $w_h$  as dynamic variables is taken into account, which is an improvement over the simulations with constant ratio  $g_c$  in [4] and [5].

The microscopic scattering rates also determine escape, capture, and scattering times for the microscopic QD system. We define  $\tau_b^{\rm cap}=1/S_b^{\rm in}$  and  $\tau_b^{\rm esc}=1/S_b^{\rm out}$  (b=e,h). The values for the scattering times  $\tau_e$  and  $\tau_h$  resulting from our microscopic calculations are depicted as dashed red and solid black lines, respectively, in Fig. 2(a). They show a decrease with the carrier

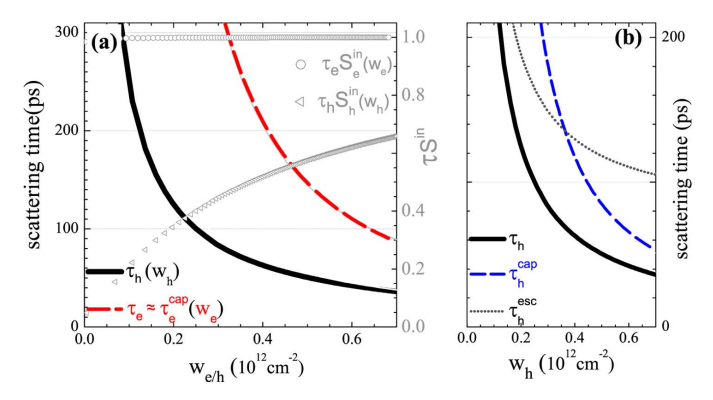


Fig. 2. Scattering times. (a) Dashed red and solid black lines show microscopically calculated electron and hole scattering times  $\tau_e$  and  $\tau_h$  of the confined QD level as a function of the WL electron density  $w_e$ . Gray symbols:  $\tau_b S_b^{\text{in}}(w_b) \ (b=e,h)$ . (b) Dashed blue and dotted gray lines show capture and escape times  $\tau_h^{\rm cap}$  and  $\tau_h^{\rm esc}$ , respectively, for holes as a function of  $w_h$ . Black solid line:  $\tau_h$ .  $g_c = w_h/w_e$  is given by (30).

density in the WL. Fig. 2(b) depicts escape, capture, and scattering times for holes plotted as dotted, dashed, and solid lines. For the electrons, only  $\tau_e$  is plotted because, due to the small escape rate of the electrons, there is only a marginal difference between  $au_e$  and  $au_e^{
m cap}$  . Several publications dealing with QD laser modeling, e.g., [10] and [11], include a linear dependence upon the WL carrier density w, such as  $S^{\rm in} = w/(\tau^{\rm cap}N^{\rm WL})$  and  $S^{\text{out}} = (N^{\text{WL}} - w)/(\tau^{\text{esc}}N^{\text{WL}})$ . Compared to our approach, this is a rough approximation. The following functions provide the best fit for the scattering times plotted in Fig. 2. Here, note that the ratio  $g_c = w_h/w_e$  is given by the steady-state relation derived in (30)

$$\tau_h^{\text{cap}} = \frac{1.5 \text{ ps} \cdot \text{nm}^{-2}}{538 \text{ nm}^2 w_h^2 + w_h} + 6 \text{ ps}$$
 (6)

$$\tau_h^{\text{esc}} = \frac{0.24 \text{ ps} \cdot \text{nm}^{-2}}{100 \text{ nm}^2 w_h^2 + w_h} + 86 \text{ ps}$$
 (7)

$$\tau_h = \frac{0.29 \,\mathrm{ps \cdot nm^{-2}}}{w_h} - 3.6 \,\mathrm{ps}$$
 (8)

$$\tau_h = \frac{0.29 \text{ ps} \cdot \text{nm}^{-2}}{w_h} - 3.6 \text{ ps}$$

$$\tau_e^{\text{cap}} \approx \tau_e = \frac{5.2 \text{ ps} \cdot \text{nm}^{-2}}{w_e + 1570 \text{ nm}^2 w_o^2} + 27 \text{ ps.}$$
(9)

It can be seen that for the hole scattering time, the dependence on  $w_h$  is close to what would be expected with the assumption of a linear scattering rate. In contrast to this, we find a more complicated functional relation for the electron scattering rate. It has to be noted that for even higher WL carrier densities, both electron and hole scattering times will finally increase due to Pauli blocking of the scattered Auger electron.

The products  $\tau_e S_e^{\text{in}}(w_e)$  and  $\tau_h S_h^{\text{in}}(w_h)$  are also plotted in Fig. 2(a), and are indicated by gray circles and triangles, respectively. Compared to the complex nonlinear dependencies of the scattering rates, these relatively simple functions for  $au_e S_e^{ ext{in}}$ and  $\tau_h S_h^{\text{in}}$  are very useful for further analysis of the rate equation system (see next section). In the following, we will derive these functions using the principle of detailed balance. In thermodynamic equilibrium, there is a detailed balance between the in- and out-scattering rates of the QD level. This allows to relate the rate coefficients of in- and out-scattering even for nonequilibrium carrier densities [17]. For a discrete two-level system with energy difference  $\Delta E$ , the escape and capture times

 $\tau^{\rm esc}$  and  $\tau^{\rm cap}$ , i.e., the inverse rate coefficients of the single electron escape and capture processes, are related by  $\tau^{\rm esc} =$  $\tau^{\rm cap} \exp(\Delta E/(kT))$  [18]. However, for the Auger scattering between the degenerate 2-D electron gas of the WL and the discrete QD level, the ratio  $(S_b^{\mathrm{in}}/S_b^{\mathrm{out}})$  also depends on the WL quasi-Fermi level  $F_b^{\text{WL}}$  for b = e and b = h.

Assuming quasi-equilibrium within the WL states but nonequilibrium between the WL electrons, and the QD electrons, the WL holes, and the QD holes, the occupation probability of electrons in the WL states  $E_k$  can be expressed by quasi-Fermi distributions

$$f_k = \left[ \exp\left(\frac{E_k - F_b^{\text{WL}}}{kT}\right) + 1 \right]^{-1}, \qquad b = e, h. \tag{10}$$

The total electron and hole densities in the respective WL are given by

$$w_e = \rho_e \int_{E_e^{\text{WL}}}^{\infty} dE_k f_k$$

$$= \rho_e k T \ln \left[ 1 + \exp\left(\frac{F_e^{\text{WL}} - E_e^{\text{WL}}}{kT}\right) \right] \qquad (11)$$

$$w_h = \rho_h \int_{-\infty}^{E_h^{\text{WL}}} dE_k (1 - f_k)$$

$$= \rho_h k T \ln \left[ 1 + \exp\left(\frac{E_h^{\text{WL}} - F_h^{\text{WL}}}{kT}\right) \right] \qquad (12)$$

with the 2-D density of states  $\rho_b = m_b/(\pi \hbar^2)$ , where  $m_b$  are the effective masses of electrons (b = e) and holes (b = h), respectively, and  $E_h^{\rm WL}$  are the WL band edges of conduction and valance bands, respectively. Equations (11) and (12) can be inverted to express the quasi-Fermi levels  $F_e^{
m WL}$  and  $F_h^{
m WL}$  as a function of the nonequilibrium WL carrier densities  $w_e$  and  $w_h$ [24]:

$$F_e^{\text{WL}}(w_e) = E_e^{\text{WL}} + kT \ln \left[ \exp \left( \frac{w_e}{\rho_e kT} \right) - 1 \right]$$
 (13)  
$$F_h^{\text{WL}}(w_h) = E_h^{\text{WL}} - kT \ln \left[ \exp \left( \frac{w_h}{\rho_h kT} \right) - 1 \right].$$
 (14)

The microscopic Auger in- and out-scattering rates are given

$$S_e^{\text{in}} = \sum_{klmb'} W_{klmb'}^{\text{in}} f_k f_l (1 - f_m) \qquad (k \to \text{QD}, l \to m)$$

$$S_e^{\text{out}} = \sum_{klmb'} W_{klmb'}^{\text{out}} (1 - f_k) (1 - f_l) f_m \qquad (\text{QD} \to k, m \to l)$$

where the transition probabilities  $W_{klmb'}^{\mathrm{in/out}}$  contain the Coulomb matrix elements and the energy-conserving  $\delta$ -function [5]. For a single electron–electron scattering process, the in-scattering rate can be rewritten as follows:

$$\begin{split} W_{klme}^{\text{in}} f_k f_l (1 - f_m) \\ &= W_{klme}^{\text{in}} (1 - f_k) (1 - f_l) f_m \frac{f_k}{1 - f_k} \frac{f_l}{1 - f_l} \frac{1 - f_m}{f_m} \\ &= W_{klme}^{\text{out}} (1 - f_k) (1 - f_l) f_m \\ &\times \exp\left(\frac{F_e^{\text{WL}} - E_k - E_l + E_m}{kT}\right) \end{split}$$

where the microscopic reversibility of the Coulomb matrix elements and the quasi-Fermi distribution given in (10), i.e.,

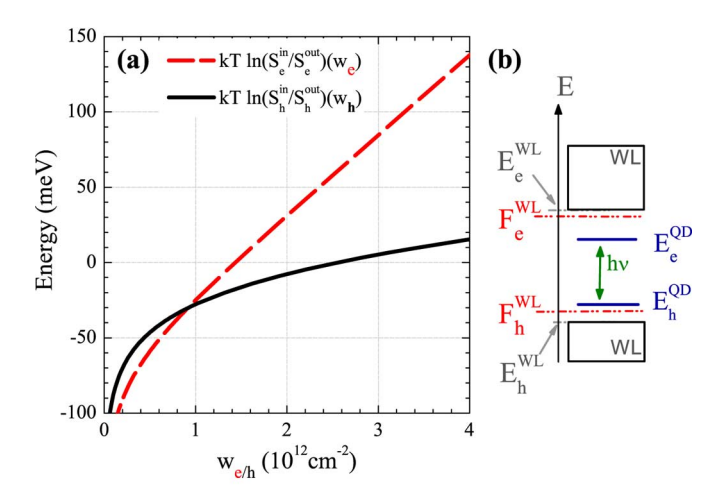


Fig. 3. Detailed balance. (a) Dashed red and solid black lines show  $kT \ln(S_b^{\rm in}/S_b^{\rm out})$  for electrons (b=e) and holes (b=h), respectively, according to the calculated scattering rates (Fig. 1) versus  $w_b$ . (b) Sketch of the energy diagram of the QD and WL system. The plot of  $F_e^{\rm WL}(w_e) - E_e^{\rm QD}$  and  $E_h^{\rm QD} - F_h^{\rm WL}(w_h)$  coincides exactly with the lines shown in (a).  $E_e^{\rm WL} - E_e^{\rm QD} \equiv \Delta E_e = 190$  meV;  $E_h^{\rm QD} - E_h^{\rm WL} \equiv \Delta E_h = 69$  meV;  $h\nu = 0.96$  eV.

 $f_k/(1-f_k)=\exp{[(F_e^{\rm WL}-E_k)/(kT)]}$ , have been used. Inserting the energy conservation of final and initial states,  $E_m-E_l-E_k+E_e^{\rm QD}=0$ , where  $E_e^{\rm QD}$  is the confined QD electron energy, and summing over all initial and final states give

$$S_e^{\rm in} = S_e^{\rm out} \exp\left(\frac{F_e^{\rm WL} - E_e^{\rm QD}}{kT}\right). \tag{15}$$

Note that (15) also holds for the mixed e-h Auger process, and an analogous relation holds for hole in- and out-scattering rates:

$$S_h^{\rm in} = S_h^{\rm out} \exp\left(\frac{E_h^{\rm QD} - F_h^{\rm WL}}{kT}\right). \tag{16}$$

In Fig. 3, the numerically calculated values of kT  $\ln\left[S_b^{\rm in}(w_b)/S_b^{\rm out}(w_b)\right]$  are plotted versus  $w_b$  for electrons and holes. They coincide exactly with  $F_e^{\rm WL}(w_e)-E_e^{\rm QD}$  and  $E_h^{\rm QD}-F_h^{\rm WL}(w_h)$  taken from (13) and (14), as predicted from the detailed balance relations from (15) and (16). For WL densities higher than  $\rho_b kT$  ( $\rho_e kT=0.47\times10^{12}$  cm<sup>-2</sup> and  $\rho_h kT=4.8\times10^{12}$  cm<sup>-2</sup>), the quasi-Fermi levels  $F_b^{\rm WL}$  given by (13) and (14) depend approximately linearly on  $w_b$  through  $F_b^{\rm WL}=E_b^{\rm WL}\pm w_b/\rho_b$ . Thus, for  $w_b>\rho_b kT$ , the curves in Fig. 3 are straight lines with a slope of  $1/\rho_b$ .

Using (15), we can rewrite

$$\tau_e S_e^{\text{in}}(w_e) = \left[\frac{S_e^{\text{out}}}{S_e^{\text{in}}} + 1\right]^{-1}$$

$$= \left[\exp\left(\frac{E_e^{\text{QD}} - F_e^{\text{WL}}(w_e)}{kT}\right) + 1\right]^{-1} \quad (17)$$

$$= \left[\frac{e^{-\Delta E_e/(kT)}}{e^{w_e/(\rho_e kT)} - 1} + 1\right]^{-1}. \quad (18)$$

Analogously,

$$\tau_h S_h^{\text{in}}(w_h) = \left[ \exp\left(\frac{F_h^{\text{WL}}(w_h) - E_h^{\text{QD}}}{kT}\right) + 1 \right]^{-1} \tag{19}$$

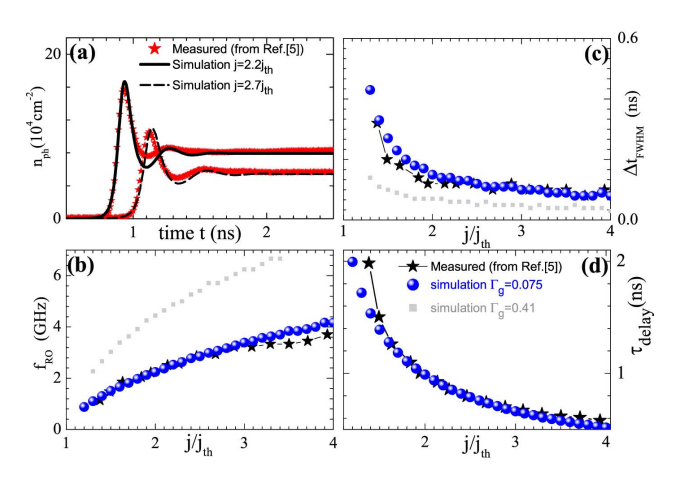


Fig. 4. (a) Comparison of experimental (taken from [5]) and simulated turn-on transients for  $j=2.2j_{\rm th}$  and  $j=2.7j_{\rm th}$ . (b)–(d) Comparison between experimental (black stars) [5] and simulated data (blue dots) plotted versus increasing pump current  $j/j_{\rm th}$ . (b) Frequency of ROs,  $f_{\rm RO}$ . (c) Width of the first RO peak,  $\Delta t_{\rm FWHM}$ . (d) Turn-on delay time,  $\tau_{\rm delay}$ . Parameters as in Table I. Gray squares in (b)–(d) show simulated results for different  $\Gamma_q=0.41$ .

$$= \left[ \frac{e^{-\Delta E_h/(kT)}}{e^{w_h/(\rho_h kT)} - 1} + 1 \right]^{-1}.$$
 (20)

In the literature, escape rates are often derived by assuming thermal equilibrium for the QD laser system [7], [25], where the WL is treated as a single discrete level with degeneracy  $g = \rho_e kT/N^{\rm QD}$ . However, this holds for the situation only where the Fermi level of the WL is equal to its band edge.

# III. ELECTRON AND HOLE DYNAMICS

Using the microscopic scattering rates as described in the previous section, we were able to simulate the gain switching dynamics of the QD laser. Moreover, we were able to quantitatively reproduce experimental results. Fig. 4(a) shows a comparison between experimental (red stars taken from [5]) [5] and simulated turn-on transients underlining the excellent agreement. Even for a wide range of different pump currents  $j/j_{\rm th}$ , the key parameters, namely the frequency of ROs,  $f_{\rm RO}$ , the width of the first RO peak,  $\Delta t_{\rm FWHM}$ , and the turn-on delay time,  $\tau_{\rm delay}$ , correspond nicely to the experimental data points, as can be seen in Fig. 4(b)–(d).

Since our model allows for a separate treatment of electron and hole dynamics, we will investigate the transient behavior of both. As can be seen in the phase portrait of Fig. 5(d), the turn-on process projected onto the  $(n_h, n_e)$ -plane deviates from a straight line (which corresponds to the synchronized behavior  $n_e \sim n_h$ ) and instead performs a spiral ending in the fixed point (steady state). This desynchronization between electron and hole dynamics is due to different effective masses and the resulting different energy separation between WL band edge and confined QD level [ $\Delta E_e = 190$  meV and  $\Delta E_h = 69$  meV, respectively, as depicted in Fig. 3(b)]. Although the in-scattering rate of holes is much higher (see Fig. 1), their out-scattering rate is comparably large, which results in a small scattering lifetime. Hence, the QD hole density reacts more slowly to dynamic changes than that of the electrons, leading to a small phase shift of both transients [see Fig. 5(b) and (c)]. Furthermore, the maximum value of the electron concentration during the RO has a larger difference in the steady-state value than that of the hole

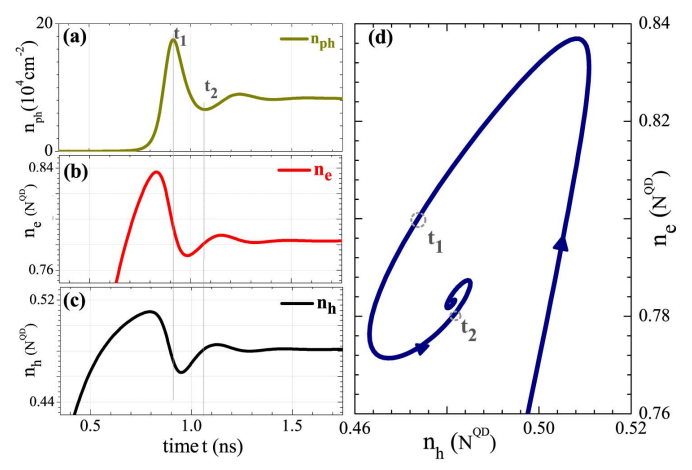


Fig. 5. Turn-on transients of (a) photon density  $n_{ph}$ ; (b) electron density in the QDs  $n_e$ ; and (c) hole density in the QDs  $n_h$  ( $n_e$  and  $n_h$  are normalized to the active QD density  $N^{\rm QD}$ ). (d) Turn-on process projected onto the  $(n_e, n_h)$ -plane.  $t_1$  and  $t_2$  mark the first maximum and the first minimum of the turn-on transient, respectively.  $j = 2.7j_{\rm th}$ . Other parameters as in Table I.

concentration. While in the steady state, most of the QDs are occupied by an electron, the holes are only half filled.

Fig. 6(a) and (b) shows the trajectories (blue lines) of the turn-on process projected onto the  $(n_b, n_{vh})$ -planes. The familiar anticlockwise rotation can be seen for the electron as well as for the hole density. Nonetheless, their shape is different, as the dynamic range of the electrons is higher, leading to a wider spiral. The black circles in Fig. 6(a) and (b) denote the steady-state values of the electron and hole concentrations  $(n_e^* \text{ and } n_h^*)$  for increasing pump current. It is interesting to note that the value of  $n_e^*$  decreases with j. This is anomalous since for conventional lasers, the carrier concentration is clamped at the threshold value (saturation of inversion). Nevertheless, the inversion is also saturated for our system as the total number of carriers, namely the threshold density  $n_t = n_e^* + n_h^*$ , is a constant that depends only on the material parameters and not on the pump current. Therefore, the steady-state values of the hole concentration in the QDs  $n_h^*$  increases with current. Neglecting spontaneous emission, it follows from the equation  $\dot{n}_{ph} = 0 \text{ [see (5)]}$ 

$$n_t = n_e^* + n_h^* = \frac{2\kappa}{\Gamma W A} + N^{\text{QD}}.$$
 (21)

As already pointed out in [5], an increase in the confinement parameter leads to higher oscillation frequencies, higher output power, lower damping rate, and lower threshold currents. In Fig. 6(c) and (d), the resulting electron and hole dynamics for a geometric confinement factor of  $\Gamma_g=0.41$  can be seen. (A higher  $\Gamma_g$  can be achieved by using more QD layers or larger QD size.) Compared to the situation for higher  $\Gamma_q$ , the dynamics of the carriers is compressed and much more synchronized than before. The steady-state values of the electron and hole density [black circles in Fig. 6(c) and (d)] shift to lower values; however, the electron density still decreases with j. The changes in the synchronization between electron and hole dynamics are again visible in Fig. 7(a) and (b), which shows turn-on transients of the electron and hole dynamics for two different  $\Gamma_g$ . As can be seen for higher  $\Gamma_q$  [Fig. 7(b)], the phase shift disappears and the dynamic range is comparable. The influence of the increased  $\Gamma_a$ on the photon output is depicted in Fig. 7(c), showing a drastic

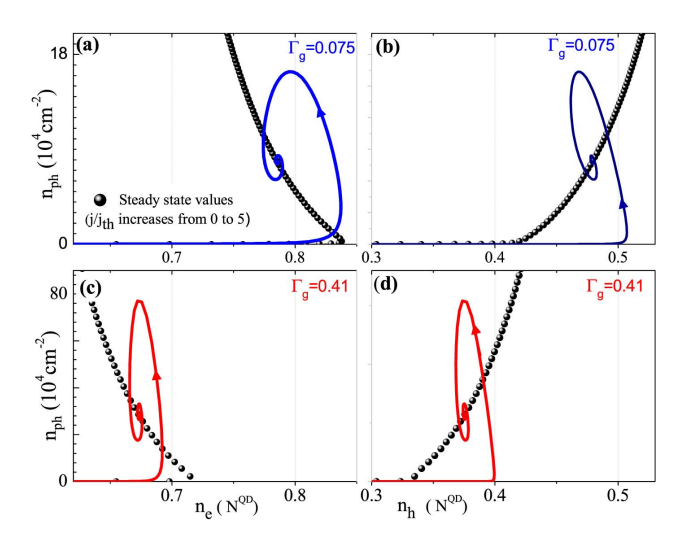


Fig. 6. Phase portrait of the turn-on dynamics in the  $(n_e, n_{ph})$ - and  $(n_h, n_{ph})$ -planes at  $j=2.6j_{\rm th}$ . (a) and (b)  $\Gamma_g=0.075$ . (c) and (d)  $\Gamma_g = 0.41$ . (Circles) Steady-state values  $n_e^*$  and  $n_h^*$  for increasing  $j \ (0 < j \le 5j_{\rm th})$ .  $n_e$  and  $n_h$  are normalized to the active QD density  $N^{\rm QD}$ . Parameters as in Table I.

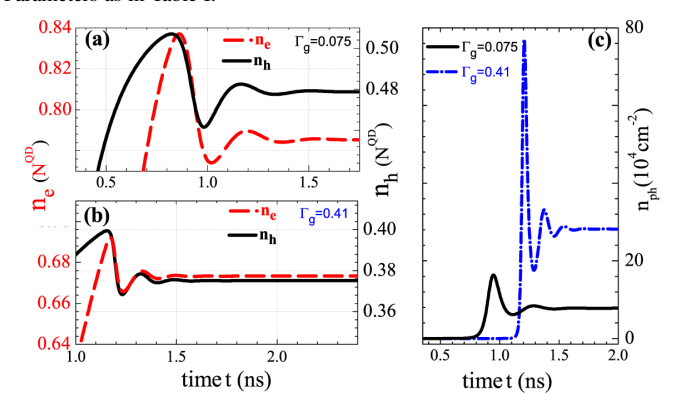


Fig. 7. Turn-on transients for (a)  $\Gamma_g=0.075$  and (b)  $\Gamma_g=0.41$ . Dashed red and solid blue lines show electron and hole densities in the QDs, respectively.  $n_e$  and  $n_h$  normalized to the active QD density  $N^{\rm QD}$ . (c) Photon density during turn-on for different confinement factors:  $\Gamma_g=0.075$  (solid black) and  $\Gamma_g=0.075$ 0.41 (dashed-dotted blue).  $j=2.6j_{\rm th}$ . Other parameters as in Table I.

increase in intensity and RO frequency and a decrease in the damping. Erneux et al. [10] also found this transition in the dynamics of a QD laser by changing the gain coefficient that is comparable to changing the confinement factor in our model. The numeric value of the RO frequency  $f_{\rm RO}$  for increased  $\Gamma_q$  is also plotted in Fig. 4(b), which shows the square-root increase with the pump current at about twice the value of the frequency for  $\Gamma_q = 0.075$ .

To clarify the observed behavior, we extract the nullclines  $\operatorname{NC}_1$  ( $\dot{n}_e = \dot{n}_h = \dot{n}_{ph} = 0$ ) given by (22) and  $\operatorname{NC}_2$  ( $\dot{w}_e = 0$ ) given by (23) of the rate equation system (1)–(5) projected onto the 2-D subspace  $(w_e, n_e)$ . The intersection of the nullclines determines the steady state. The nullclines are given by

$$\frac{n_e(w_e, w_h)}{N^{\text{QD}}} = \frac{2\kappa/(\Gamma W A N^{\text{QD}} \tau_h) + \left(S_e^{\text{in}} + S_h^{\text{out}}\right)}{S_e^{\text{in}} + S_e^{\text{out}} + S_h^{\text{in}} + S_h^{\text{out}}} 
= \frac{(n_t/N^{\text{QD}})\tau_e + \left(\tau_h \tau_e S_e^{\text{in}} - \tau_e \tau_h S_h^{\text{in}}\right)}{\tau_e + \tau_h} (22) 
\frac{n_e(w_e, w_h, j)}{N^{\text{QD}}} = \tau_e S_e^{\text{in}} - \frac{\tau_e}{N^{\text{sum}}} \left(\frac{\eta}{e_0} j - B^S w_e w_h\right). (23)$$

$$\frac{n_e(w_e, w_h, j)}{N^{\text{QD}}} = \tau_e S_e^{\text{in}} - \frac{\tau_e}{N^{\text{sum}}} \left(\frac{\eta}{e_0} j - B^S w_e w_h\right). \quad (23)$$

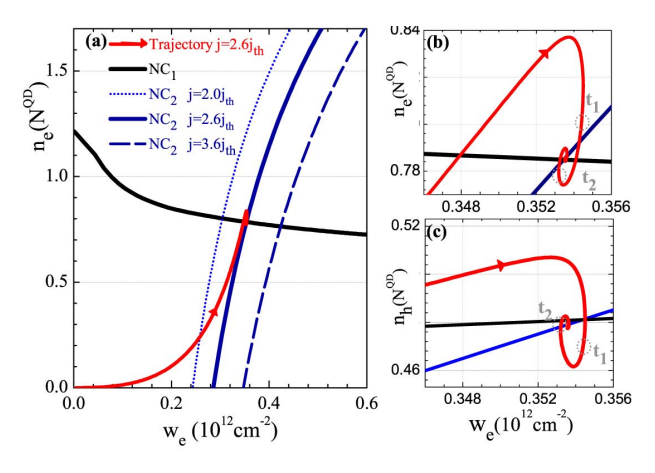


Fig. 8. (a) Nullcline  $\mathrm{NC}_1$  [(22)] and  $\mathrm{NC}_2$  [(23)] are indicated by solid black and blue lines, respectively, in  $(n_e,w_e)$ -plane. Dotted solid and dashed blue lines correspond to  $\mathrm{NC}_2$  for different pump currents:  $j=2.0j_{\mathrm{th}},j=2.6j_{\mathrm{th}}$ , and  $j=3.6j_{\mathrm{th}},n_e$  is normalized to the QD density  $N^{\mathrm{QD}}$ . Parameters as in Table I. The trajectory of the turn-on process at  $j=2.6j_{\mathrm{th}}$  (red) is indicated by arrows. (b) Enlargements of (a) around the steady state. (c) Enlargement of the same regime but for holes in  $(n_h,w_e)$ -plane. Dotted circles denoted by  $t_1$  and  $t_2$  mark the first maximum and the first minimum of the photon turn-on transient, respectively.

Analogously, we find the nullclines for the hole density in the QDs as a function of the WL hole density by using (21) and (22), and for the first nullcline  $NC_1^h$ , which is given by (25), and  $\dot{w}_h = 0$  for the second nullcline  $NC_2^h$ , given by (25)

$$\frac{n_h(w_e, w_h)}{N^{\text{QD}}} = \frac{n_t}{N^{\text{QD}}} - \frac{n_e(w_e, w_h)}{N^{\text{QD}}}$$
(24)

$$\frac{n_h(w_e, w_h, j)}{N^{\text{QD}}} = \tau_h S_h^{\text{in}} - \frac{\tau_h}{N^{\text{sum}}} \left(\frac{\eta}{e_0} j - B^S w_e w_h\right). \tag{25}$$

The shape of the nullclines is mainly determined by the nonlinear scattering rates. Since we also consider the mixed e-hAuger processes, the scattering rates  $S_b^{\rm in/out}$  depend on both  $w_e$  and  $w_h$ . The ratio  $g_c = w_h/w_e$  changes significantly with the pump current [5] so that both nullclines implicitly depend on the current. However, in Section IV, we show that at steady state, we can derive an expression for  $q_c(w_e)$ , which then eliminates all implicit current dependence. This has been done in Fig. 8, where the nullclines  $NC_1$  [see (22)] and  $NC_2$  [see (23)] are depicted.  $NC_2$  [see (23)] is shown for three different pump currents  $(j = 2.0j_{th}, j = 2.6j_{th}, \text{ and } j = 3.6j_{th})$  while NC<sub>1</sub> [see (22)] does not depend on j any more. With increasing current, the fixed point shifts downward on  $NC_1$  to lower  $n_e$ , explaining the decrease in  $n_e^*$  with j that was already observed in Fig. 6(a); however, we can now quantify the slope as given in (23). If equal electron and hole scattering times are considered, (23) reduces to  $n_e = n_t/2$ , thus displaying a horizontal line in  $(n_e, w_e)$ -phase plane.

In addition to the nullclines, Fig. 8(a) shows the corresponding trajectories of the turn-on process (red) for  $j=2.6j_{\rm th}$  (same as in Fig. 6(a) and (c) but in a different 2-D subspace). The trajectories approach their steady-state value, which is the intersection of the two nullclines. Because the electron density  $n_e$  cannot exceed  $N^{\rm QD}$ , the intersection will always stay below  $N^{\rm QD}$  although a single nullcline can enter the forbidden region. Besides the scattering times  $\tau_e$  and  $\tau_h$ , the nullcline  $NC_1$  [(22)] is given by the parameters that determine the threshold carrier

density  $n_t$  [see (21)]. Thus, their impact on the steady state can be seen easily, e.g., an increase in  $\Gamma$  leads to a smaller  $n_t$ , and thus, to a downshift of  $NC_1$  [(22)]. As a result, reduced steady-state value for the QD carrier densities are obtained in accordance with the numeric values shown in Fig. 6(c)–(d). Fig. 8(b) and (c) shows an enlargement around the fixed point in  $(n_e, w_e)$ -plane and  $(n_h, w_e)$ -plane, respectively. They show that while the carrier density in the QDs oscillates, the WL carrier density increases monotonically. The first slope of the trajectory in  $(n_e, w_e)$ -plane that builds up the population inversion is mainly given by  $NC_2$  [(23)], which is dominated by the scattering time  $\tau_e$ . For Fig. 8(c), the nullclines  $NC_1^h$  [(25)] and  $NC_2^h$  [(25)] have been plotted together with the trajectory in the  $(n_h, w_e)$ -phase space to emphasize the hole dynamics.

For much lower scattering times, which can be obtained by using much smaller energy separation  $\Delta E_e$  and  $\Delta E_h$  between the WL and the QD levels, the nullcline  $\mathrm{NC}_2$  [(23)] is mainly given by the product  $\tau_e S_e^\mathrm{in}$ , which has a value close to 1 for  $w_e > \rho_e kT$  [see (18)]. As a result, the electrons are strongly constrained by the limit  $n_e < N^\mathrm{QD}$  and forced to closely follow the null-isocline  $\mathrm{NC}_2$  [(23)]. The holes instead would perform large-amplitude oscillations in the phase plane. For such small energy separation, the laser would show much higher damping than the case discussed here.

#### IV. LASER CHARACTERISTICS AND STEADY-STATE BEHAVIOR

Further insight into the electron and hole dynamics can be gained by deriving the functional dependence of the steady-state values upon the injection current density j. The first point of interest is the change of the steady-state value of the WL electron density as a function of pump current  $w_e^*(j)$ . This fixed point  $w_e^*(j)$  is given by the intersection of  $\mathrm{NC}_1$  [(22)] and  $\mathrm{NC}_2$  [(23)], yielding (26) that depends on  $w_e^*$  and  $w_b^*$ :

$$\frac{\eta}{e_0} j - B^S g_c w_e^{*2} 
= \frac{N^{\text{sum}}}{\tau_e(w_e^*) + \tau_h(g_c w_e^*)} \left( \tau_e S_e^{\text{in}} + \tau_h S_h^{\text{in}} - \frac{n_t}{N^{\text{QD}}} \right).$$
(26)

In order to solve this equation for  $w_e^*$ , we still have to derive a functional dependence for  $g_c(w_e^*)$ . This can be done with the help of a conservation law embedded in the rate equation system (1)–(5), which reads  $N^{\rm QD}(\dot{w}_e-\dot{w}_h)=N^{\rm WL}(\dot{n}_e-\dot{n}_h)$ . Integrating this equation for the case without external doping leads to

$$N^{\text{QD}}(w_h^* - w_e^*) = N^{\text{sum}}(n_e^* - n_h^*). \tag{27}$$

To obtain an equation for the WL carrier densities, we substitute (23) and (25) into (27) and neglect the current-dependent term

$$\frac{w_h^* - w_e^*}{N^{\text{sum}}} = \tau_e S_e^{\text{in}} - \tau_h S_h^{\text{in}} - \frac{\tau_e - \tau_h}{e_o N^{\text{sum}}} (\eta j - e_o \tilde{R}_{\text{sp}})$$
 (28)

$$g_c \approx \frac{N^{\text{sum}}}{w_e^*} \left( \tau_e S_e^{\text{in}}(w_e^*) - \tau_h S_h^{\text{in}}(g_c w_e^*) \right) + 1$$
 (29)

$$g_c \approx 0.87 + 0.62 \frac{N^{\text{sum}}}{w_e^*}.$$
 (30)

Since (29) depends solely on  $w_e^*$  and  $g_c$ , this gives the desired dependence  $g_c(w_e^*)$ . Through the products  $\tau_b S_b^{\text{in}}$ , the ratio  $g_c$  depends on the effective masses and the energy separations

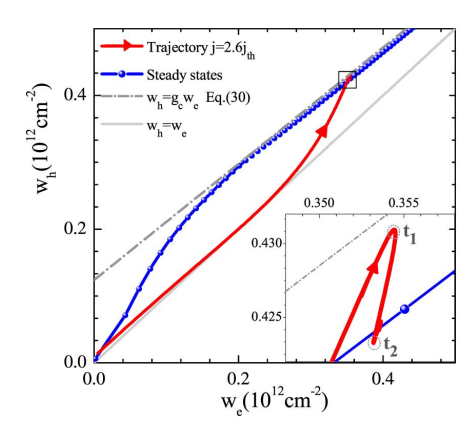


Fig. 9. Relation between WL electron and hole densities in  $(w_e, w_h)$ -plane: dashed-dotted gray line shows  $w_e^*g_c$  as given by (29). Blue circles show the steady-state values resulting from numeric integration. Solid gray line denotes  $w_e = w_h$ . Red line with arrow is the trajectory of the laser turn-on. (Inset) Close-up around fixed point for  $j=2.6j_{\rm th}$ . Dotted circles denoted by  $t_1$  and  $t_2$  mark the first maximum and the first minimum of the turn-on transient, respectively. Parameters as in Table I.

 $\Delta E_e$  and  $\Delta E_h$ . The dashed-dotted gray line in Fig. 9 depicts  $w_h^* = g_c(w_e^*)w_e^*$ . It can be seen that it is a good approximation compared to the actual steady-state values  $w_h^*(w_e^*)$  plotted as blue circles in the  $(w_e, w_h)$ -plane. Fig. 9 also shows the trajectory of the turn-on process as a red line with arrow. The excursion through the phase space, where both carrier types increase and finally approach their steady state, takes part during the delay time  $\tau_{\rm delay}$ . The maximum photon output is reached at the turning point of the trajectory. The inset in Fig. 9 shows a close-up of the phase space region where it can be seen that compared to the steady-state value, the WL carrier densities do not change much during the ROs (circles at  $t_1$  and  $t_2$  in the inset denote the first maximum and minimum of the turn-on transient, respectively). Using the solution of (29) and substituting it into (26), we arrive at the steady-state solution  $w_e^*(j)$ . It gives very good result compared to the numeric integration of the full system. Fig. 10(b) shows the steady-state values  $w_e^*(j)$ and  $w_b^*(j)$  as solid red and dashed black curves. They perform a square-root-like increase with the current j. From (26), we see that this increase is determined by the spontaneous emission in the WL  $(R_{\rm sp} = B^S w_e w_h)$  as long as  $1/(\tau_e + \tau_h)$  is small, and thus, for high scattering times as used for our modeling. We therefore find the analytic approximation

$$w_e^*(j) \approx \sqrt{\frac{j}{B^S g_c}} + 10 \text{ ps } j.$$
 (31)

For smaller scattering times, which can be obtained with smaller energy separations  $\Delta E_e$  and  $\Delta E_h$ , the solution of (26) would be dominated by the scattering rates and would thus yield a smaller value for  $w_e^*$ .

Using the approximations (31) for  $w_e^*(j)$  and (30) for  $g_c$  to yield  $w_h^*(j)$ , the steady-state values of  $n_e^*(j)$  and  $n_h^*(j)$  are given by NC<sub>2</sub> [(23)] and NC<sub>2</sub><sup>h</sup> [(25)]. The results for the steady-state values found by numeric integration are plotted in Fig. 10(a), together with the analytic approximation. As

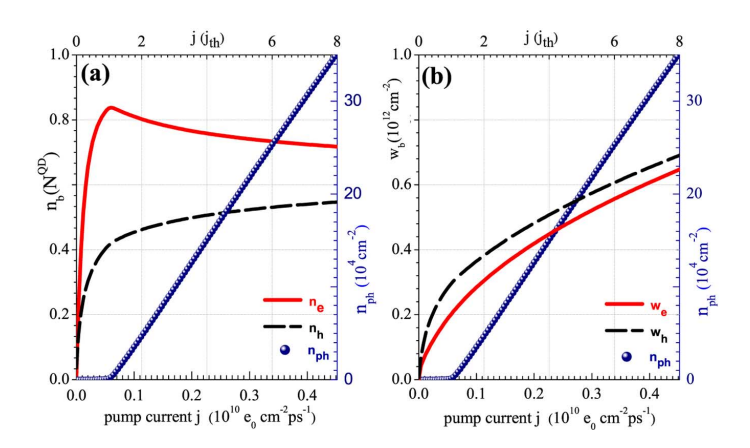


Fig. 10. Steady states. (a) Solid red and dashed black lines show steady-state values of electron and hole density in the QDs,  $n_e^*(j)$  and  $n_h^*(j)$ , respectively, as a function of pump current. Blue circles show  $n_{ph}^*(j)$ , which gives the threshold current  $j_{\rm th}$  at which lasing starts. (b) Same as (a) but for the carrier densities in the WL,  $w_e^*(j)$  and  $w_h^*(j)$ . Parameters as in Table I.

already discussed before, using Fig. 6, the steady-state value of the electron density  $n_e^*(j)$  decreases with the current while  $n_b^*(j)$  increases.

Additionally, Fig. 10(a) and (b) also depicts the input–output characteristic, i.e.,  $n_{ph}^*(j)$  of the laser by blue circles. Using (5) with  $\beta \approx 0$ , (3), and (1) in the steady state, we arrive at a laser characteristic described by

$$n_{ph}^*(j) = \eta \frac{\Gamma}{2\kappa e_o} \frac{N^{\text{QD}}}{N^{\text{sum}}} (j - j_{\text{th}}^*)$$
 (32)

where

$$\frac{\eta}{e_o} j_{\rm th}^* = B^S w_e^* w_h^* + \frac{W N^{\rm sum}}{(N^{\rm QD} N^{\rm QD})} n_e^* n_h^*. \tag{33}$$

It shows the linear increase with the pump current j as seen in Fig. 10. It has to be noted that  $j_{\rm th}^*$  is not a constant but depends on j through the carrier densities in the WL and QD. The parameter  $w_e$  at threshold, and therefore, the threshold current  $j_{\rm th}$  can be determined by solving (34) for  $w_e$  with  $g_c$  given by (29). The resulting values of  $w_e^{th}=0.21\times 10^{12}~{\rm cm}^{-2}$  and  $j_{\rm th}/e_o=5.7\times 10^8~{\rm cm}^{-2}\cdot{\rm ps}^{-1}$  agree well with the values found by numeric integration

$$W\tau_{e}S_{e}^{\text{in}}\left(1 - \tau_{e}W\tau_{h}S_{h}^{\text{in}}\right)\left(\frac{n_{t}}{N^{\text{QD}}} - \tau_{e}S_{e}^{\text{in}}(1 - \tau_{e}W\tau_{h}S_{h}^{\text{in}})\right)$$

$$= \frac{1}{\tau_{e} + \tau_{h}}\left(\tau_{e}S_{e}^{\text{in}} + \tau_{h}S_{h}^{\text{in}} - \frac{n_{t}}{N^{\text{QD}}}\right). \quad (34)$$

By using the steady-state WL carrier density given by (31) and the numeric values resulting from (34), the input-output characteristic (32) can be approximated by

$$n_{ph}^*(j) \approx 0.13 \frac{\Gamma}{2\kappa e_o} \frac{N^{\text{QD}}}{N^{\text{sum}}} (j - j_{\text{th}}).$$
 (35)

## V. CONCLUSION

In conclusion, we have found that the nonlinearity of the scattering rates and the inclusion of separate dynamics of holes and electrons are crucial in order to explain the dynamic behavior of a QD laser. We have derived a detailed balance formula connecting the nonequilibrium in- and out-scattering Auger rates via a WL carrier density depending factor. Moreover, we have derived the steady-state characteristic and found analytic expressions for the dependence of the dynamic variables on the pump current in the steady state.

#### ACKNOWLEDGMENT

The authors thank T. Erneux, A. Knorr, E. Malic, and N. Majer for fruitful discussions.

#### REFERENCES

- [1] D. Bimberg, M. Grundmann, and N. N. Ledentsov, *Quantum Dot Heterostructures*. New York: Wiley, 1999.
- [2] W. W. Chow and S. W. Koch, *Semiconductor-Laser Fundamentals*. Berlin, Germany: Springer-Verlag, 2004.
- [3] E. Malić, K. J. Ahn, M. J. P. Bormann, P. Hövel, E. Schöll, A. Knorr, M. Kuntz, and D. Bimberg, "Theory of relaxation oscillations in semiconductor quantum dot lasers," *Appl. Phys. Lett.*, vol. 89, pp. 101107-1–101107-3, 2006.
- [4] E. Malić, M. J. P. Bormann, P. Hövel, M. Kuntz, D. Bimberg, A. Knorr, and E. Schöll, "Coulomb damped relaxation oscillations in semiconductor quantum dot lasers," *IEEE J. Sel. Topics Quantum Electron.*, vol. 13, no. 5, pp. 1242–1248, Sep./Oct. 2007.
- [5] K. Lüdge, M. J. P. Bormann, E. Malić, P. Hövel, M. Kuntz, D. Bimberg, A. Knorr, and E. Schöll, "Turn-on dynamics and modulation response in semiconductor quantum dot lasers," *Phys. Rev. B*, vol. 78, no. 3, pp. 035316-1–035316-11, 2008.
- [6] T. R. Nielsen, P. Gartner, and F. Jahnke, "Many-body theory of carrier capture and relaxation in semiconductor quantum-dot lasers," *Phys. Rev. B*, vol. 69, pp. 235314-1–235314-13, 2004.
- [7] D. G. Deppe and H. Huang, "Fermi's golden rule, nonequilibrium electron capture from the wetting layer, and the modulation response in p-doped quantum-dot lasers," *IEEE J. Quantum Electron.*, vol. 42, no. 3/4, pp. 324–330, Mar. 2006.
- [8] K. Veselinov, F. Grillot, C. Cornet, J. Even, A. Bekiarski, M. Gioannini, and S. Loualiche, "Analysis of the double laser emission occurring in 1.55 μm InAs–InP (113)B quantum-dot lasers," *IEEE J. Quantum Electron.*, vol. 43, no. 9, pp. 810–816, Sep. 2007.
- [9] M. Gioannini and I. Montrosset, "Numerical analysis of the frequency chirp in quantum-dot semiconductor lasers," *IEEE J. Quantum Elec*tron., vol. 43, no. 10, pp. 941–949, Oct. 2007.
- [10] T. Erneux, E. A. Viktorov, and P. Mandel, "Time scales and relaxation dynamics in quantum-dot lasers," *Phys. Rev. A*, vol. 76, pp. 023819-1–023819-7, 2007.
- [11] A. Fiore and A. Markus, "Differential gain and gain compression in quantum-dot lasers," *IEEE J. Quantum Electron.*, vol. 43, no. 4, pp. 287–294, Apr. 2007.
- [12] A. E. Viktorov, P. Mandel, A. G. Vladimirov, and U. Bandelow, "Model for mode locking of quantum dot lasers," *Appl. Phys. Lett.*, vol. 88, pp. 201102-1–201102-3, 2006.
- [13] M. Lorke, F. Jahnke, and W. W. Chow, "Excitation dependences of gain and carrier-induced refractive index," *Appl. Phys. Lett.*, vol. 90, pp. 051112-1–051112-3, 2007.
- [14] H. C. Schneider, W. W. Chow, and S. W. Koch, "Excitation-induced dephasing in semiconductor quantum dots," *Phys. Rev. B*, vol. 70, no. 23, pp. 235308-1–235308-4, 2004.
- [15] W. W. Chow and S. W. Koch, "Theory of semiconductor quantum-dot laser dynamics," *IEEE J. Quantum Electron.*, vol. 41, no. 4, pp. 495–505, Apr. 2005.

- [16] E. A. Viktorov, P. Mandel, J. Houlihan, G. Huyet, and Y. Tanguy, "Electron-hole asymmetry and two-state lasing in quantum dot lasers," *Appl. Phys. Lett.*, vol. 87, no. 5, pp. 053113-1–053113-3, 2005.
- [17] E. Schöll, Nonequilibrium Phase Transitions in Semiconductors. Berlin, Germany: Springer-Verlag, 1987.
- [18] P. T. Landsberg, Recombination in Semiconductors. Cambridge, U.K.: Cambridge Univ. Press, 1991.
- [19] D. O'Brien, S. P. Hegarty, G. Huyet, and A. V. Uskov, "Sensitivity of quantum-dot semiconductor lasers to optical feedback," *Opt. Lett.*, vol. 29, no. 10, pp. 1072–1074, 2004.
- [20] T. Piwonski, I. O'Driscoll, J. Houlihan, G. Huyet, R. J. Manning, and A. V. Uskov, "Carrier capture dynamics of InAs/GaAs quantum dots," *Appl. Phys. Lett.*, vol. 90, pp. 122108-1–122108-3, 2007.
  [21] H. Dery and G. Eisenstein, "The impact of energy band diagram and
- [21] H. Dery and G. Eisenstein, "The impact of energy band diagram and inhomogeneous broadening on the optical differential gain in nanostructure lasers," *IEEE J. Quantum Electron.*, vol. 41, no. 1, pp. 26–35, Jan. 2005.
- [22] E. Gehrig and O. Hess, "Mesoscopic spatiotemporal theory for quantum-dot lasers," *Phys. Rev. A*, vol. 65, no. 3, pp. 033804-1–033804-16, 2002.
- [23] C. Xing and E. A. Avrutin, "Multimode spectra and active mode locking potential of quantum dot lasers," *J. Appl. Phys.*, vol. 97, pp. 104301-1–104301-9, 2005.
- [24] E. Schöll, A. Amann, M. Rudolf, and J. Unkelbach, "Transverse spatio-temporal instabilities in the double barrier resonant tunneling diode," *Physica B*, vol. 314, pp. 113–116, 2002.
- Physica B, vol. 314, pp. 113–116, 2002.
  [25] H. Jiang and J. Singh, "Nonequilibrium distribution in quantum dots lasers an influence on laser spectral output," *J. Appl. Phys.*, vol. 85, no. 10, pp. 7438–7442, 1999.



**Kathy Lüdge** was born in Berlin, Germany, in 1976. She received the Diploma and the Dr. rer. nat. degree in physics from the Technische Universität Berlin, Germany, in 2000 and 2003, respectively, within the Department of Solid State Physics.

From 2001 to 2002, she was a Visiting Scholar with the Department of Material Science, University of Minnesota, Minneapolis, MN. Her research interests include modeling of semiconductor quantum dot lasers, nonlinear laser dynamics, and control with optical feedback.



Eckehard Schöll was born on February 6, 1951 in Stuttgart, Germany. He received his Diplom degree in physics (M.Sc.) from the University of Tübingen, Germany, in 1976, the Ph.D. degree in applied mathematics from the University of Southampton, U.K., in 1978, and the Dr. rer. nat. degree and the venia legendi from Aachen University of Technology (RWTH Aachen), Germany, in 1981 and 1986, respectively.

During 1983–1984 he was a Visiting Assistant Professor in the Department of Electrical and Computer Engineering, Wayne State University,

Detroit, Michigan. Since 1989, he has been a Professor of Theoretical Physics at Technische Universität (TU) Berlin. Since 2001, he has been the Director of the Institute for Theoretical Physics at TU Berlin. His research interests include nonlinear dynamics, pattern formation, chaos, noise, control, theory of transport in semiconductor nanostructures, laser dynamics, and self-organized growth kinetics. He is the author of about 350 research papers and three books, and the editor of several monographs and topical journal issues.

Dr. Schöll was the organizer of several international conferences including Dynamics Days Europe in 2005, and the 72nd Annual German Physical Society Meeting in 2008.